

# Synthesis and Unveiling the Effect of Nonmagnetic Zn<sup>2+</sup> Ions on Enrichment of Structural Properties of Barium-Nickel Ferrites

Sadiq.H. Khoreem<sup>1,2,3\*</sup> , A. H. Al-Hammadi<sup>1</sup>, W.F. AL-Eryani<sup>3</sup> 

<sup>1</sup> Physics Department, Faculty of Science, Sana'a University, Sana'a, Yemen

<sup>2</sup> Department of Optometry and Vision Science, Faculty of Medical Sciences, Al-Razi University, Sana'a, Yemen

<sup>3</sup> Physics Department, Faculty of Science, Saada University, Saada, Yemen

\* Correspondence: khoreems@yahoo.com, sadiqkhoreem@alraziuni.edu.ye (S.H.K.);

Scopus Author ID 57571836200

Received: 2.09.2022; Accepted: 7.10.2022; Published: 6.01.2023

**Abstract:** The effects of zinc substitution on barium-based and nickel-based hexagonal ferrites have been investigated. The ceramic technique prepared three series of hexagonal ferrites with nominal compositions, BaNi<sub>2-x</sub>Zn<sub>x</sub>Fe<sub>16</sub>O<sub>27</sub> (x = 0.0, 0.4, 0.8, 1.2, 1.6, 2.0). The powder samples' structural properties have been investigated using the X-ray diffraction (XRD) technique. X-ray diffraction (XRD) patterns of samples confirm the single phase w-type hexagonal structure with p63/mmc space group. The average crystallite size of ferrites was within the range of 35 -36 nm. The lattice constant was increased with the increase in zinc concentration in all samples. Bulk density increased with the increase in zinc concentration in all sample ferrites, whereas X-ray density decreased with the increase in zinc concentration in all sample ferrites. Though the constant lattice increases, the increase in mass follows up with the increase in volume, so X-ray density increases. Porosity decreased with the increase in zinc concentration in all samples. The decrease in the surface area may be due to the increase in crystallite size. The ferrimagnetic materials with crystallite size lower than 50 nm can be potentially employed for the reduction of signal-to-noise ratio in numerous high-density recording and microwave applications. Tetrahedral bond length, octahedral bond length, tetrahedral edge, and shared and unshared octahedral edges increase as the Zn<sup>2+</sup> content x increases. This could be related to the larger radius of Zn<sup>2+</sup> ions as compared with Ni<sup>2+</sup> ions.

**Keywords:** crystal structure; barium-nickel ferrites-lattice parameters; structural parameters.

© 2023 by the authors. This article is an open-access article distributed under the terms and conditions of the Creative Commons Attribution (CC BY) license (<https://creativecommons.org/licenses/by/4.0/>).

## 1. Introduction

The ferrites materials possess a crystalline structure having magnetic nature and high resistivity. The ferrites are gaining substantial interest among the research community because of better efficiency, low cost, and suitable dielectric loss; therefore, they find prospective applications in microwave and memory cores devices. These synthesis compositions can also be widely used in transformer cores, data storage, inductor, microwave devices, computer memory chips, antenna rods, etc. [1]. Ferrites exhibit excellent properties when the size of the particles approaches the nano range [2]. At the nanoscale, ferrites revealed excellent dielectric as well as magnetic properties. Therefore, curiosity in ferrites is increasing increasingly with the progress of nanotechnology. Various innovative assets of ferrites can be modified for utilization in magnetic storage, as magnetically guided delivery agents drugs, and as precursors

for ferrofluids, etc. Therefore, structural, electrical, magnetic, and dielectric properties also can be enhanced by controlling the particle size. Ferrite systems such as  $\text{BaNi}_2\text{Cr}_x\text{Fe}_{16-x}\text{O}_{27}$ , and  $\text{BaZn}_x\text{Co}_{1-x}\text{Fe}_{16}\text{O}_{27}$ , are very significant for high-tech applications [3,4]. Ni–Zn bulk ferrite nanomaterials are the only core materials applicable to high-frequency applications [5-8].

The main drawback is that its performance is constrained to higher frequencies due to eddy current at high frequencies. The increased grain generates grain boundaries that behave as a barrier for electron flow, causing a reduction in the eddy current losses [9–11].

Also, doping of Ba-Ni by Zn ions ferrite has significant attention owing to their interesting and enhancement properties of the ferrites. Here, we discuss Zn ions' influence on Ba-Ni nano ferrites. This research aims to investigate the role of Zn substitution on the structural properties of Ba-Ni ferrites. The successful experimental approach will open a new gateway for improving devices based on BaNi-Zn ferrites, which are used in surface mount devices (SMD) and multilayer chip inductors (MLCI) due to their high electrical resistivity and soft magnetic properties at high frequencies. These devices are used in electronic applications such as telecommunication. These devices' efficiency depended on the materials' structural, electrical and magnetic properties. The possible reasons responsible for the substitution dependence of main structural properties have been discussed. Systematic research is still necessary for a more comprehensive understanding of and properties of such materials.

## 2. Materials and Methods

A composition sample of the  $\text{BaNi}_{2-x}\text{Zn}_x\text{Fe}_{16}\text{O}_{27}$  w-type ferrite system (with  $x=0.0, 0.4, 0.8, 1.2, 1.6, \text{ and } 2$ ) has been prepared using the usual ceramics method as mentioned earlier [12,13]. The schematic flow chart of synthesis is shown in Figure.1. Final powders have been obtained after final sintering at  $950\text{ }^\circ\text{C}$  for 8 hours. Powder X-ray diffraction patterns were recorded at room temperature. This facility was availed by the Yemen Geological Survey and Mineral Resources Board (YGSMRB), the model (Shimadzu EDX-720) diffractometer for the determination of lattice constant and crystal structure of the prepared compounds. The sample was used in powdered form; the powder was placed in a plate shape ( $20\times 18\text{ mm}^2$ ) sample holder ( $35\times 50\text{ mm}^2$ ) made of aluminum [14]. The powder of each sample was placed one by one. The monochromatic beam of X-rays  $\text{CuK}\alpha$  ( $\lambda=1.5406\text{ \AA}$ ) radiations was generated at a point, and the intensity of the diffracted beam was detected with a counter. The X-rays pattern was obtained for each composition by changing the angle  $2\theta$  from  $5^\circ$  to  $75^\circ$  at a step size of  $0.04^\circ$  per second. The source was operating under an accelerating voltage of  $40\text{ kV}$  with a tube current of  $20\text{ mA}$ . A continuous scan was done with a constant scanning rate of  $0.02/1\text{ sec}$ .

## 3. Results and Discussion

### 3.1. XRD studies.

Barium-Nickel ferrites with chemical formula  $\text{BaNi}_{2-x}\text{Zn}_x\text{Fe}_{16}\text{O}_{27}$  for  $x$  ranging from  $0.0$  to  $2.0$  with the step increment of  $0.4$  were prepared by the standard ceramic method. The variation of Zn substitution has a significant effect on the structural properties. The synthesis materials have been characterized by their grain size, sintered density, lattice constant, X-ray density, and porosity. X-ray powder diffraction of the samples was carried out at room temperature using a PANalytical diffractometer system with  $\text{CuK}\alpha$  ( $\lambda = 1.5406\text{ \AA}$ ) radiations to check the formation of the required product and related structural properties. The indexed XRD patterns for all the samples corresponding to the system  $\text{BaNi}_{2-x}\text{Zn}_x\text{Fe}_{16}\text{O}_{27}$  are shown in

Figure.1. These patterns confirm the formation of a single-phase w-type hexagonal structure. It was observed that all the samples are in good accordance with the BaNi<sub>2</sub> W-type hexaferrite structure of p63/mmc. Zn-doped BaNi<sub>2-x</sub>Zn<sub>x</sub>Fe<sub>16</sub>O<sub>27</sub> is consistent with standard powder diffraction data of JCPDS,54-0097. The Full-Proof software and MDI-Jade software were used in the XRD profile fitting by applying space group P63/mmc (No. 194).

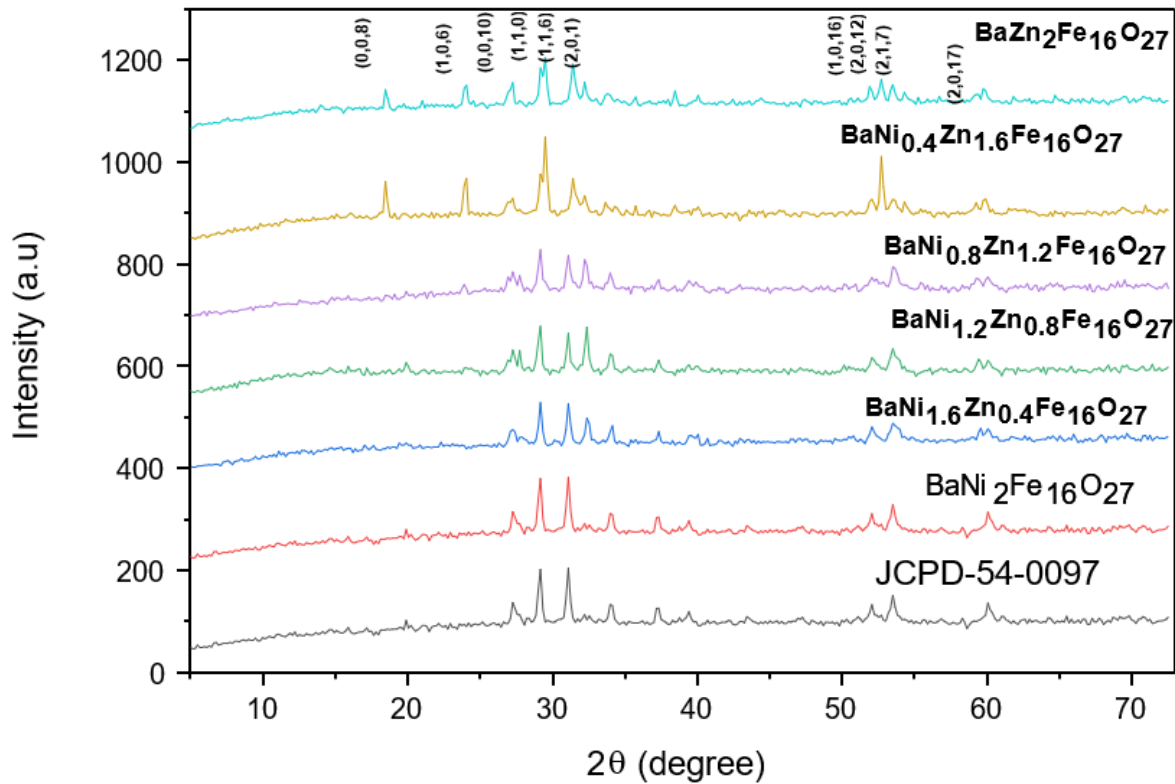


**Figure 1.** XRD patterns for BaNi<sub>2-x</sub>Zn<sub>x</sub>Fe<sub>16</sub>O<sub>27</sub> (x = 0, 0.4, 0.8, 1.2, 1.6, 2) W-type hexaferrite.

The lattice constants a and c were calculated by indexing the XRD patterns using equation 1[12]:

$$\frac{1}{d_{hkl}^2} = \frac{4h^2 + hk + k^2}{3a^2} + \frac{L^2}{C^2} \quad (1)$$

It is noticed from Figure 2 a,b. that both lattice constants a and c increase with the increase of Zn concentration. It is due to the ionic radius of Zn<sup>2+</sup> (0.74Å) being larger than that of Ni<sup>2+</sup> ion (0.69Å), as reported by [15,16]. Also, since the ionic radius of Zn<sup>2+</sup> (0.74 Å) is greater than that of Ni<sup>2+</sup>(0.68 Å) and since the unit cell expands when the substituted cation size is larger, so, the increase in the lattice constant can be attributed to the differences in the size of the cations [17]. Also, the increment of Zn<sup>2+</sup> ions in Ni-ferrite causes the Fe<sup>3+</sup> ions to migrate from the A site to the B site. These larger ions, Zn<sup>2+</sup> (0.74 Å) than Fe<sup>3+</sup> ions (0.67 Å) and Ni<sup>2+</sup> ions (0.68 Å), make the A sites, and thus the lattice expands, increasing the lattice parameter. Moreover, the value of parameters c/a of hexagonal W-type structure is between 5.33-5.55 [18]. Figure 2c show the value of c/a in our samples fitted well into this range, which implied that the magnetoplumbite structure was formed. The crystallite size is calculated by using Scherrer equation 2:

$$D = k\lambda / \beta_{hkl} \cos\theta \quad (2)$$

where λ = 1.5406 Å is the wavelength of X-ray diffraction, θ is Bragg's diffraction angle, k is the shape factor, its value is 0.9, while β<sub>hkl</sub> is full width at half maximum (FWHM). Figure 2d Shows variations in crystallite size with an increase in zinc contents. Initially, the crystallite

size of barium-based ferrites ( $\text{BaNi}_{2-x}\text{Zn}_x\text{Fe}_{16}\text{O}_{27}$ ) for  $x = 0.0$  was 36.5nm, and with zinc substitution ( $x=0.4$ ), crystallite size decreased to 35.18nm. Then gradually increased to reach 36.7nm as zinc concentration increased up to  $x= 2$ . This increase in crystallite size with zinc concentration shows that nickel act as a crystallite inhibitor. This is in agreement with [19].

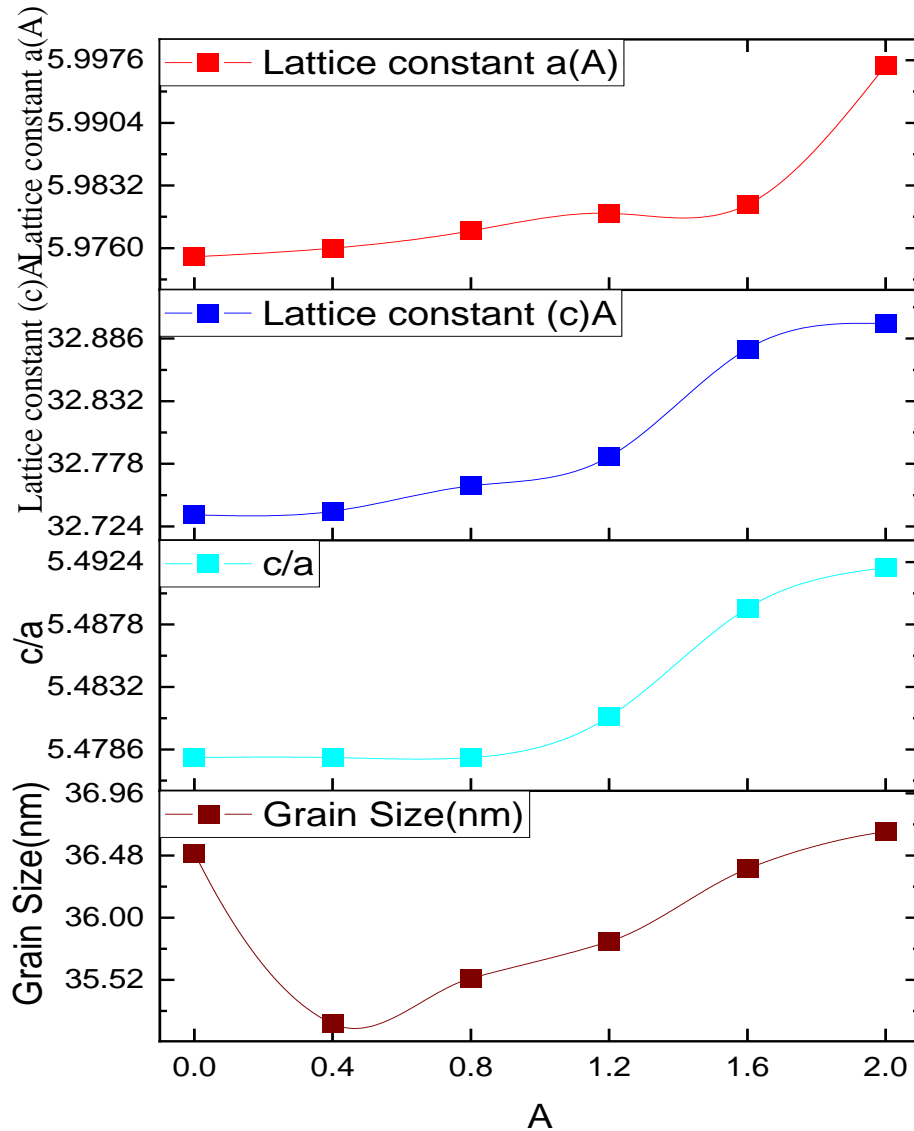


**Figure 2.** The relation between (a): lattice parameters (a), (b): lattice parameters, (c): ratio (c/a), (d): Crystallite size and  $\text{Zn}^{2+}$  concentration for  $\text{BaNiZnFe}_{16}\text{O}_{27}$ .

### 3.2. Experimental density.

The experimental density  $\rho_s$  was calculated by equation 3:

$$\rho_B = \frac{m}{\pi r^2 h} \tag{3}$$

where m, r, and h are the mass, the radius, and the thickness (height) of the pellet, respectively. The experimental density was increased from 4.189  $\text{g/cm}^3$  to 4.62  $\text{g/cm}^3$  with the enhancement of doped concentration (Zn), as shown in Figure 3b. This increase in experimental density is due to the difference in ionic radii between Ni and Zn. Also, this increase may be due to the higher density of zinc (8.96  $\text{g/cm}^3$ ) than that of nickel (8.90  $\text{g/cm}^3$ ). Similar behavior has been reported by others [20,21].

### 3.3. X-ray density.

The X-rays density ( $\rho_x$ ) of the samples was calculated using equation 4 given by Smit and Wijn [22].

$$\rho_x = \frac{ZM}{N_A V} \tag{4}$$

where Z represents the number of molecules per unit cell, Z has a value of 2 of W-type hexagonal ferrites, M is the molecular weight of the sample,  $N_A$  is Avogadro's number ( $6.02 \times 10^{23}$  g/mol), and V is the unit cell volume.

Figure 3a shows the results of x-ray density. It was decreased from 5.375 g/cm<sup>3</sup> to 5.235 g/cm<sup>3</sup> with an increase in Zn concentration, as given in Figure 3a X-rays density depends upon the lattice constant this result could be understood by equation 4, which increased x-ray density with the increase in Zn<sup>2+</sup> ions concentration, which may be due to the increase in lattice constant, so the corresponding X-rays density decreased with the increase in Zn concentration. The molar mass of Ni is less than Zn, and the unit cell volume (V) increased with the increase of Zn ions concentration doping. It proved that zinc ions had entered the lattice successfully. A similar trend has been reported by [21]. Table.1 shows that the lattice constant increased with the increase in zinc concentration, so the corresponding X-ray density decreased with the increase in Zn concentration.

### 3.4. Porosity.

The relative porosity (%P) of the samples has been calculated from x-ray density and experimental density by using equation 5.

$$\%P = \left( \frac{\rho_x - \rho_B}{\rho_x} \right) \times 100 \tag{5}$$

The porosity is a crucial parameter when deciding the magnetic susceptibility of the samples. Figure 3c show the porosity with Zn concentration which was tabulated in Table 1. It is observed that as the concentration of zinc increases, porosity decreases. This is due to Zn's larger ionic radius than Ni. As depicted in Figure 3c, the porosity decreased from 0.354 to 0.102 with increasing Zn ions concentration, which should be expected because of the above reasons. The creation of more oxygen vacancies with increased Zn doped in the samples and, as a result, few cations are created. This is another reason leading to decreased porosity [23]. It was noted that the porosity behavior was opposite to bulk density. The composition  $x = 0.0$  has the highest bulk density and lowest porosity. It is observed that the X-ray density of each sample is larger than the corresponding sintered density. This may be due to the existence of pores in the samples. Similar kinds of results have been reported by others [21].

### 3.5. Specific surface area.

The specific surface area (S) for the synthesis compositions were calculated by using equation 6 [24]:

$$S = \frac{6000}{D \rho_x} \tag{6}$$

The variation of specific surface area (S) as a function of Zn ions concentration was shown in Figure 3 d. It indicates an increasing trend with ( $x=0.4$ ). The rise in the surface area could also be because of the reduction in crystallite size. This means the smaller the crystallite size, the bigger is the number of surface atoms, and therefore the larger the surface area. After

that decreased with increasing Zn concentration, the surface area decrease may be due to the increase in crystallite size. When the crystallite size becomes larger, these will become the number of surface atoms, and the smaller will be the surface area. When the crystallite size is small, the surface area is bigger, indicating that the number of atoms at the surface is greater, i.e., when the surface covered by atoms at the material's surface is more relevant when the crystallite size is small. The ferrimagnetic materials with crystallite size of fewer than fifty nanometers ( $D < 50\text{nm}$ ) may be potentially utilized to reduce signal/noise ratio in various high-density recording and microwave applications.

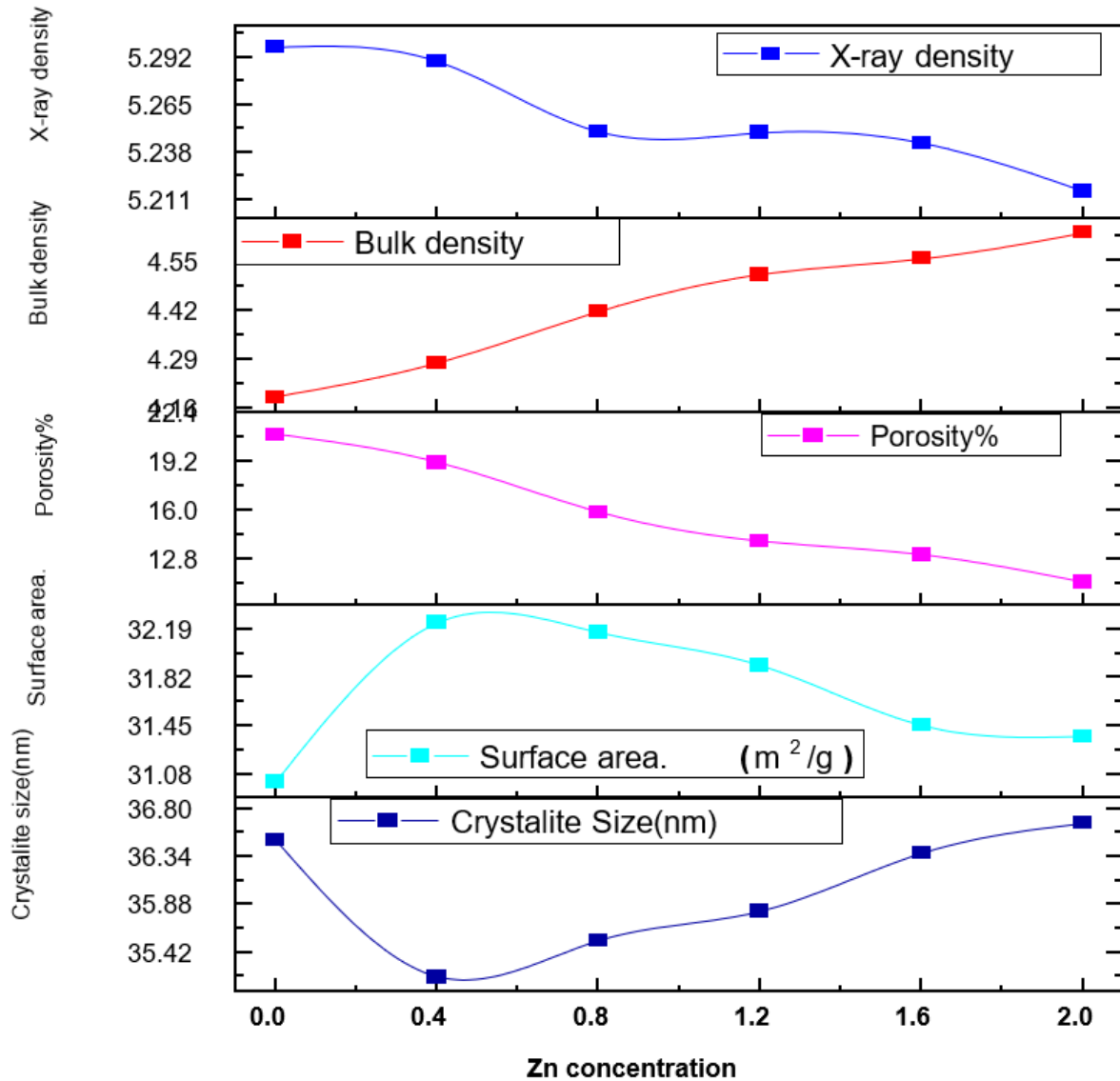


**Figure 3.** The relation between (a): X-ray density, with Zn concentration for  $\text{BaNi}_{2-x}\text{Zn}_x\text{Fe}_{16}\text{O}_{27}$  (b): bulk density with Zn concentration for  $\text{BaNi}_{2-x}\text{Zn}_x\text{Fe}_{16}\text{O}_{27}$ , (c): porosity, with Zn concentration for  $\text{BaNi}_{2-x}\text{Zn}_x\text{Fe}_{16}\text{O}_{27}$ , (d): surface area, with  $\text{Zn}^{2+}$  concentration for  $\text{BaNi}_{2-x}\text{Zn}_x\text{Fe}_{16}\text{O}_{27}$ .

Though the constant lattice increases, the increase in mass follows up the increase in volume, and therefore X-ray density increases.

The distance between magnetic ions and the hopping lengths in tetrahedral sites ( $L_A$ ) and octahedral sites ( $L_B$ ) were also calculated using the relation (7-8) [25,26] and are given in Table.1. and also presented graphically in Figure 4a shows the relation between the hopping lengths in octahedral and tetrahedral sites as a function of Zn content.

$$L_A = 0.25a\sqrt{3} \tag{7}$$

$$L_B = 0.25a\sqrt{2} \tag{8}$$

The calculated values of  $L_A$  and  $L_B$  are given in Table 1, and Figure 4b shows the relation between the hopping lengths in octahedral and tetrahedral sites with Zn content. It is observed that the hopping length increases as the  $Zn^{2+}$  ions content increases. The behavior of hopping length with zinc-doped concentration may be due to the lattice's constant variation with the zinc content. In other words, the increase in distance between the magnetic ions increases with an increase in the zinc concentration. This may be explained based on the difference in ionic radii. This may be ascribed to the fact that  $Ni^{2+}$  ion has a smaller radius (0.68 Å) than  $Zn^{2+}$  ion, i.e. (0.74 Å). Also, the enlargement of the unit cell is caused by doping relatively bigger zinc ions instead of smaller nickel ions. Hence, the distance between the magnetic ions increases as the Zn content increases.

Using the experimental values of lattice parameter  $a$ , oxygen positional parameter  $u$  ( $u = 0.381$  Å) and by using the equation 9-10, tetrahedral and octahedral bond lengths  $d_{Ax}$  and  $d_{Bx}$ , tetrahedral edge, were calculated [27,28]. Also, shared and unshared octahedral edges ( $d_{AxE}$ ,  $d_{BxE}$ , and  $d_{BxEU}$ ) were calculated using equations 11, 12, and 13 [29,30], and the values are arranged as in Table 2 and also presented graphically in Figure 4.

$$d_{Ax} = a\sqrt{3}\left(u - \frac{1}{4}\right) \tag{9}$$

$$d_{Bx} = a\left[3u^2 - \left(\frac{11}{4}\right)u + \left(\frac{43}{64}\right)\right]^{\frac{1}{2}} \tag{10}$$

$$d_{AxE} = a\sqrt{2}\left(2u - \frac{1}{2}\right) \tag{11}$$

$$d_{BxE} = a\sqrt{2}(1 - 2u) \tag{12}$$

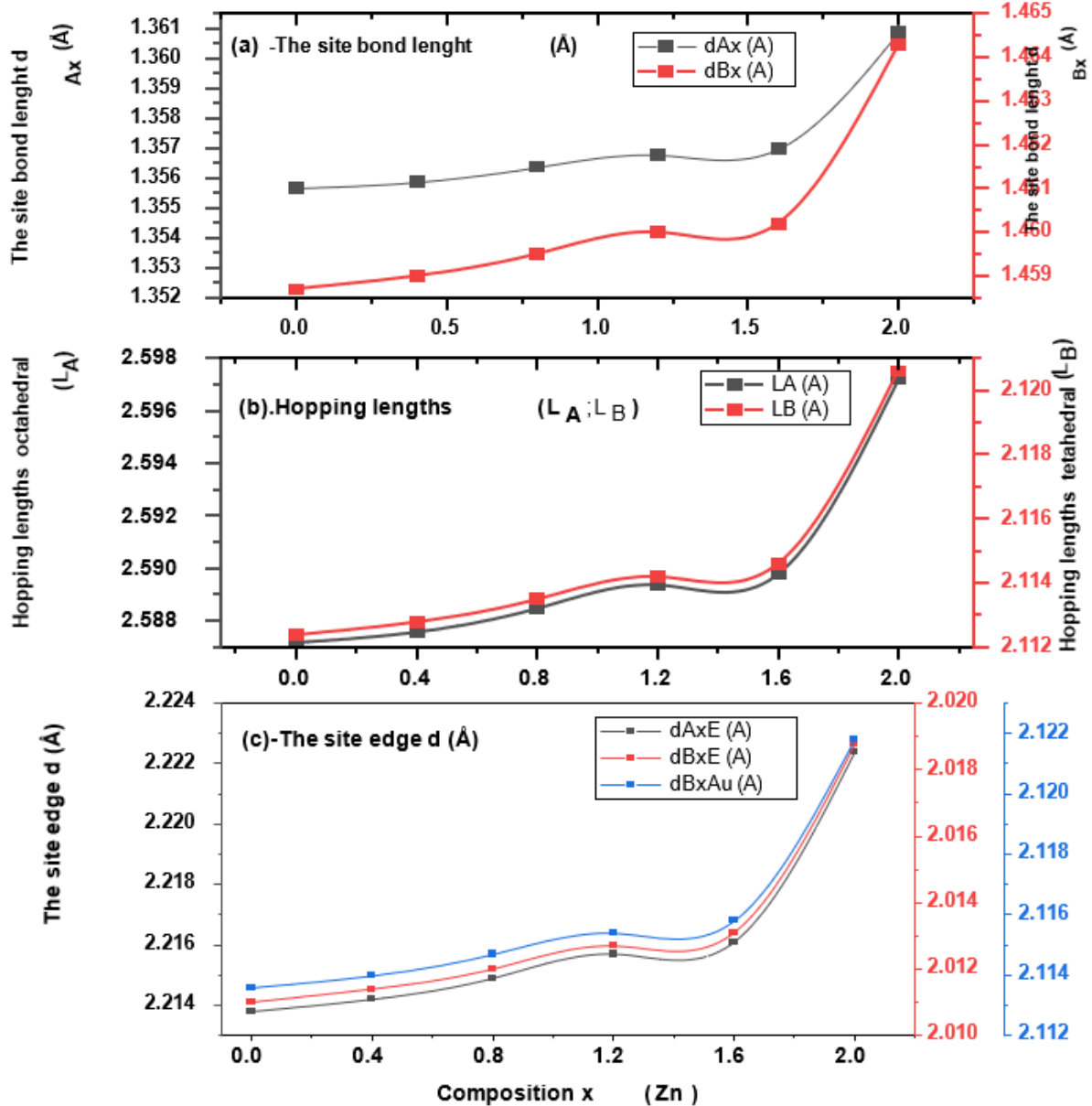
$$d_{BxEU} = a\left[4u^2 - 3u + \left(\frac{11}{6}\right)\right]^{\frac{1}{2}} \tag{13}$$

Table 1 indicates that tetrahedral bond length, octahedral bond length, tetrahedral edge, and shared and unshared octahedral edges increase as the  $Zn^{2+}$  content  $x$  increases. This could be related to the larger radius of  $Zn^{2+}$  ions as compared with  $Ni^{2+}$  ions.

**Table 1.** Hopping length ( $L_A$ ) and ( $L_B$ ), tetrahedral bond length ( $d_{Ax}$ ), octahedral bond length ( $d_{Bx}$ ), tetrahedral edge ( $d_{AxE}$ ), shared ( $d_{BxE}$ ) and unshared ( $d_{BxEU}$ ) octahedral edges as a function of  $Zn^{2+}$  concentration.

X (Zn)	a (Å)	Hopping length		Edges				
		$L_A$ (Å)	$L_B$ (Å)	$d_{Ax}$ (Å)	$d_{Bx}$ (Å)	$d_{AxE}$ (Å)	$d_{BxE}$ (Å)	$d_{BxEU}$ (Å)
0	5.975	2.5872	2.1124	1.3557	1.4587	2.2138	2.0110	2.1136
0.4	5.976	2.5876	2.1128	1.3559	1.4590	2.2142	2.0114	2.1140
0.8	5.978	2.5885	2.1135	1.3564	1.4595	2.2149	2.0120	2.1147
1.2	5.98	2.5894	2.1142	1.3568	1.4600	2.2157	2.0127	2.1154
1.6	5.981	2.5898	2.1146	1.3570	1.4602	2.2161	2.0131	2.1158
2	5.998	2.5972	2.1206	1.3609	1.4643	2.2224	2.0188	2.1218

Figure 4a indicates that the tetrahedral bond length  $d_{Ax}$  increases as Zn content  $x$  increases, and the octahedral bond length  $d_{Bx}$  decreases. Figure 4c shows that the tetrahedral edge  $d_{AxE}$ , unshared octahedral edge  $d_{BxEU}$ , and shared octahedral edge  $d_{BxE}$  increase with an increase in the dopant concentration of zinc. This increase may be related to Zn's larger ion radius than small Ni ions and the fact that nonmagnetic Zn occupies a strongly tetrahedral A-site while the magnetic Ni occupies an octahedral B-site.



**Figure 4.** (a) Variation of hopping lengths in octahedral ( $L_A$ ) with tetrahedral ( $L_B$ ) sites with the Zn content  $x$  of the series  $BaNi_{2-x}Zn_xFe_{16}O_{27}$ . (b) Tetrahedral  $d_{Ax}$  and octahedral  $d_{Bx}$  bond lengths with Zn content  $x$  of the series  $BaNi_{2-x}Zn_xFe_{16}O_{27}$ . (c) Tetrahedral edge  $d_{AxE}$ , shared  $d_{BxE}$ , and unshared  $d_{BxEU}$  octahedral edge with Zn content  $x$  of the series  $BaNi_{2-x}Zn_xFe_{16}O_{27}$ .

#### 4. Conclusions

The composition  $BaNi_{2-x}Zn_xFe_{16}O_{27}$  ( $x = 0, 0.4, 0.8, 1.2, 1.6, \text{ and } 2$ ) has been successfully synthesized by a ceramic method. The effect of  $Zn^{2+}$  ion doping on the microstructure properties of the samples has been studied. Based on observations and experiments, it is concluded that the substitution of Zn ions in  $BaNi_{2-x}Zn_xFe_{16}O_{27}$  ferrites produces appreciable changes in its structural properties. The characteristic peaks of W-type barium ferrite were found in XRD patterns, confirming the single-phase hexagonal structure, which matched well with the standard card pattern (JCPDS card No.54-0097). The lattice constants,  $a$ , and  $c$ , were found to increase with the increase in Zn ions dopant concentration due to the larger ionic radius of  $Zn^{2+}$  ions compared to that of  $Ni^{2+}$  ions. The crystallite size was to increase and reached the maximum value of 36 nm as the  $Zn^{2+}$  ions concentration increased. The bulk density increases with the increase in Zn concentration. This is due to the

ionic difference between  $\text{Ni}^{2+}$  and  $\text{Zn}^{2+}$  ions. At the same time, X-ray density and porosity decrease with the increase in Zn concentration. The porosity decreased as opposed to bulk density behavior. Though the constant lattice increases, the increase in mass follows up the increase in volume, so X-ray density increases. The variation of surface area as a function of Zn ions concentration was shown as an increasing trend with ( $x=0.4$ ). The increase in Specific surface area (S) may be due to the reduction in crystallite size. The smaller the crystallite size, the greater will be the number of surface atoms, and the larger will be the surface area after that decreases with increasing Zn concentration. The decrease in the surface area may be due to the increase in crystallite size and the increase of Zn ions. Tetrahedral bond length, octahedral bond length, tetrahedral edge, and shared and unshared octahedral edges increase as the  $\text{Zn}^{2+}$  ions content increases. This could be related to the larger radius of  $\text{Zn}^{2+}$  ions as compared with  $\text{Ni}^{2+}$  ions.

## Funding

This research received no external funding.

## Acknowledgments

The authors appreciate and are thankful for the contribution of the reviewers in improving the quality of the paper. In addition, the authors are most grateful to the head of the Physics Department at the Faculty of Sciences, Sana'a University-Yemen, and the Yemen Geological Survey and Mineral Resources Board (YGSMRB).

## Conflicts of Interest

The authors declare no conflict of interest.

## References

1. Algude, S.G.; Patange, S.M.; Shirsath, S.E.; Mane, D.R.; Jadhav, K.M. Elastic Behaviour of  $\text{Cr}^{3+}$  Substituted Co-Zn Ferrites. *Journal of Magnetism and Magnetic Materials* **2014**, *350*, 39–41, <https://doi.org/10.1016/j.jmmm.2013.09.021>.
2. Rana, G.; Dhiman, P.; Kumar, A.; Vo, D.-V.N.; Sharma, G.; Sharma, S.; Naushad, Mu. Recent Advances on Nickel Nano-Ferrite: A Review on Processing Techniques, Properties and Diverse Applications. *Chemical Engineering Research and Design* **2021**, *175*, 182–208, <https://doi.org/10.1016/j.cherd.2021.08.04>.
3. Rehman, A. ur; Shaukat, S.F.; Haidyrah, A.S.; Akhtar, M.N.; Ahmad, M. Synthesis and Investigations of Structural, Magnetic and Dielectric Properties of Cr-Substituted W-Type Hexaferrites for High Frequency Applications. *J Electroceram* **2021**, *46*, 93–106, <https://doi.org/10.1007/s10832-021-00246-7>.
4. Sagayaraj, R.; Dhineshkumar, T.; Prakash, A.; Aravazhi, S.; Chandrasekaran, G.; Jayarajan, D.; Sebastian, S. Fabrication, Microstructure, Morphological and Magnetic Properties of W-Type Ferrite by Co-Precipitation Method: Antibacterial Activity. *Chemical Physics Letters* **2020**, *759*, 137944, <https://doi.org/10.1016/j.cplett.2020.137944>.
5. Mitrović, N.S.; Nedeljković, B.; Obradović, N. Magnetic Features of MnZn Ferrite for Electronic Applications. *Program and the Book of abstracts / Serbian Ceramic Society Conference Advanced Ceramics and Application IX: New Frontiers in Multifunctional Material Science and Processing, Serbia, Belgrade, 20-21. September 2021* **2021**, 59–59, <https://dais.sanu.ac.rs/handle/123456789/11901>.
6. Khan, S.B.; Irfan, S.; Lee, S.-L. Influence of Zn<sup>2+</sup> Doping on Ni-Based Nanoferrites; ( $\text{Ni}_{1-x}\text{Zn}_x\text{Fe}_2\text{O}_4$ ). *Nanomaterials* **2019**, *9*, 1024, <https://doi.org/10.3390/nano9071024>.
7. Kumar, A.M.; Rao, K.S.; Varma, M.C.; Rao, K.H. Investigations of Surface Spin Canting in Ni-Zn Nanoferrite and Its Development as Magnetic Core for Microwave Applications. *Journal of Magnetism and Magnetic Materials* **2019**, *471*, 262–266, <https://doi.org/10.1016/j.jmmm.2018.09.060>.

8. Thakur, P.; Taneja, S.; Chahar, D.; Ravelo, B.; Thakur, A. Recent Advances on Synthesis, Characterization and High Frequency Applications of Ni-Zn Ferrite Nanoparticles. *Journal of Magnetism and Magnetic Materials* **2021**, *530*, 167925 <https://doi.org/10.1016/j.jmmm.2021.167925>.
9. Ahmed, M.A.; Okasha, N.; El-Dek, S.I. Preparation and Characterization of Nanometric Mn Ferrite via Different Methods. *Nanotechnology* **2008**, *19*, 065603, <https://doi.org/10.1088/0957-4484/19/6/065603>.
10. Andalib, P.; Harris, V.G. Grain Boundary Engineering of Power Inductor Cores for MHz Applications. *Journal of Alloys and Compounds* **2020**, *832*, 153131, <https://doi.org/10.1016/j.jallcom.2019.153131>.
11. Gegevičius, R.; Franckevičius, M.; Gulbinas, V. The Role of Grain Boundaries in Charge Carrier Dynamics in Polycrystalline Metal Halide Perovskites. *Eur. J. Inorg. Chem.* **2021**, *2021*, 3519–3527, <https://doi.org/10.1002/ejic.202100360>.
12. Al-Hammadi, A.H.; Khoreem, S.H. Investigations on Optical and Electrical Conductivity of Ba/Ni/Zn/Fe<sub>16</sub>O<sub>27</sub> Ferrite Nanoparticles. *Biointerface Res Appl Chem* **2022**, *13*, 168, <http://dx.doi.org/10.33263/BRIAC132.168>.
13. Al-Hammadi, A.H.; Khoreem, S.H. Influence of Zn<sup>+2</sup> Doping on Dielectric Properties of Ba-Based Nanoferrites. *Biointerface Res Appl Chem.* **2022**, *13*, 265, <http://dx.doi.org/10.33263/BRIAC133.256>.
14. Aranda, R.M.; Ternero, F.; Lozano-Pérez, S.; Montes, J.M.; Cuevas, F.G. Capacitor Electrical Discharge Consolidation of Metallic Powders—A Review. *Metals* **2021**, *11*, 616, <https://doi.org/10.3390/met11040616>.
15. Hoque, S.M.; Choudhury, Md.A.; Islam, Md.F. Characterization of Ni–Cu Mixed Spinel Ferrite. *Journal of Magnetism and Magnetic Materials* **2002**, *251*, 292–303, [https://doi.org/10.1016/S0304-8853\(02\)00700-X](https://doi.org/10.1016/S0304-8853(02)00700-X).
16. Chhantbar, M.C.; Modi, K.B.; Joshi, H.H. Compositional, Temperature and Frequency Dependence of Dielectric Behaviour of Zinc Substituted Copper- Ferri-Chromates. *J Mater Sci* **2007**, *42*, 6989–6995, <https://doi.org/10.1007/s10853-006-1240-z>.
17. Almessiere, M.A.; Slimani, Y.; Auwal, I.A.; Shirsath, S.E.; Gondal, M.A.; Sertkol, M.; Baykal, A. Biosynthesis Effect of Moringa Oleifera Leaf Extract on Structural and Magnetic Properties of Zn Doped Ca-Mg Nano-Spinel Ferrites. *Arabian Journal of Chemistry* **2021**, *14*, 103261, <https://doi.org/10.1016/j.arabjc.2021.103261>.
18. Tahir, W.; Khan, M.A.; Gulbadan, S.; Majeed, A.; Mahmood, K. Comprehensive Study of Structural, Physical, and Spectroscopic Properties of Co-Ni Substituted BaMg<sub>2</sub>Fe<sub>16</sub>O<sub>27</sub> W-Type Hexaferrites. *Journal of Taibah University for Science* **2021**, *15*, 1196–1209, <https://doi.org/10.1080/16583655.2022.2025692>.
19. Mosavat, S.H.; Bahrololoom, M.E.; Shariat, M.H. Electrodeposition of Nanocrystalline Zn–Ni Alloy from Alkaline Glycinate Bath Containing Saccharin as Additive. *Applied Surface Science* **2011**, *257*, 8311–8316, <https://doi.org/10.1016/j.apsusc.2011.03.017>.
20. Valenzuela, R. Novel Applications of Ferrites. *Physics Research International* **2012**, *2012*, 1–9, <https://doi.org/10.1155/2012/591839>.
21. Ghazanfar, U.; Siddiqi, S.A.; Abbas, G. Structural Analysis of the Mn–Zn Ferrites Using XRD Technique. *Materials Science and Engineering: B* **2005**, *118*, 84–86, <https://doi.org/10.1016/j.mseb.2004.12.018>.
22. Xavier, S.; Jose, D.; George, S.; Alekha, K.V. Structural and Magnetic Characterization of Transition Metal Substituted Ferrite Nanoparticles.; Kothamangalam, India, **2020**; p. 060007, <https://aip.scitation.org/doi/abs/10.1063/5.0017047>.
23. Zhao, J.; Li, F.; Wei, H.; Ai, H.; Gu, L.; Chen, J.; Zhang, L.; Chi, M.; Zhai, J. Superior Performance of ZnCoOx/Peroxymonosulfate System for Organic Pollutants Removal by Enhancing Singlet Oxygen Generation: The Effect of Oxygen Vacancies. *Chemical Engineering Journal* **2021**, *409*, 128150, <https://doi.org/10.1016/j.cej.2020.128150>.
24. Modified Structural and Magnetic Properties of Ni-Mn-Zn Ferrite Nanoparticles Doped with Ce<sup>3+</sup>-Ions. *Biointerface Res Appl Chem* **2021**, *12*, 5021–5030, <https://doi.org/10.33263/BRIAC124.50215030>.
25. Shitole, J.B.; Keshatti, S.N.; Rathod, S.M.; Jadhav, S.S. Y<sup>3+</sup> Composition and Particle Size Influenced Magnetic and Dielectric Properties of Nanocrystalline Ni<sub>0.5</sub>Cu<sub>0.5</sub>Y<sub>x</sub>Fe<sub>2</sub>-XO<sub>4</sub> Ferrites. *Ceramics International* **2021**, *47*, 17993–18002, <https://doi.org/10.1016/j.ceramint.2021.03.114>.
26. Shitole, J.B.; Keshatti, S.N.; Rathod, S.M.; Jadhav, S.S. Y<sup>3+</sup> Composition and Particle Size Influenced Magnetic and Dielectric Properties of Nanocrystalline Ni<sub>0.5</sub>Cu<sub>0.5</sub>Y<sub>x</sub>Fe<sub>2</sub>-XO<sub>4</sub> Ferrites. *Ceramics International* **2021**, *47*, 17993–18002, <https://doi.org/10.1016/j.ceramint.2021.03.114>.
27. Rather, S.; Saeed, U.; Al-Zahrani, A.A.; Bamufleh, H.S.; Alhumade, H.A.; Taimoor, A.A.; Lemine, O.M.; Ali, A.M.; Al Zaitone, B.; Alam, M.M. Doped Nanostructured Manganese Ferrites: Synthesis,

- Characterization, and Magnetic Properties. *Journal of Nanomaterials* **2021**, 2021, 1–12, <https://doi.org/10.1155/2021/9410074>.
28. Priyadharshini, P.; Pushpanathan, K. TUNING OF CRYSTALLITE SIZE, ENERGY GAP, AND MAGNETIC PROPERTY OF Mn-DOPED CoFe<sub>2</sub>O<sub>4</sub> NANOPARTICLES. *Surf. Rev. Lett.* **2021**, 28, 2150052, <https://doi.org/10.1142/S0218625X21500529>.
  29. Peng, Y.; Xia, C.; Cui, M.; Yao, Z.; Yi, X. Effect of Reaction Condition on Microstructure and Properties of (NiCuZn)Fe<sub>2</sub>O<sub>4</sub> Nanoparticles Synthesized via Co-Precipitation with Ultrasonic Irradiation. *Ultrasonics Sonochemistry* **2021**, 71, 105369, <https://doi.org/10.1016/j.ultsonch.2020.105369>.
  30. Khatun, N.; Hossain, M.S.; Begum, Most.H.A.; Islam, S.; Tanvir, N.I.; Bhuiyan, R.H.; Al-Mamun, Md. Effect of Sintering Temperature on Structural, Magnetic, Dielectric and Optical Properties of Ni–Mn–Zn Ferrites. *J. Adv. Dielect.* **2021**, 11, 2150028, <https://doi.org/10.1142/S2010135X21500284>.